

JGR Space Physics

RESEARCH ARTICLE

10.1029/2024JA033463

Key Points:

- We present the spatial evolution and parametric dependence of different ion kinetic instabilities within the Earth's magnetosheath
- Conditions for the mirror-mode instability exhibit a higher prevalence near the subsolar magnetopause compared to the flank regions
- Conditions for the oblique firehose instability are more prominent near the bow shock region than in the vicinity of the magnetopause

Correspondence to:

H. Li and W. Jiang,
hli@nssc.ac.cn;
jiangwence@swl.ac.cn





Citation:

Jiang, W., Li, H., Yang, Z., Verscharen, D., & Wang, C. (2025). Spatial dependence of ion-kinetic instabilities in the Earth's magnetosheath: MMS observations. *Journal of Geophysical Research: Space Physics*, 130, e2024JA033463. <https://doi.org/10.1029/2024JA033463>

Received 21 OCT 2024

Accepted 18 FEB 2025

Spatial Dependence of Ion-Kinetic Instabilities in the Earth's Magnetosheath: MMS Observations

Wence Jiang¹ , Hui Li^{1,2} , Zhongwei Yang^{1,2}, Daniel Verscharen³ , and Chi Wang^{1,2} 

¹State Key Laboratory of Space Weather, National Space Science Center, CAS, Beijing, China, ²University of Chinese Academy of Sciences, Beijing, China, ³Mullard Space Science Laboratory, University College London, Dorking, UK

Abstract The Earth's magnetosheath plasma frequently exhibits unequal temperatures parallel and perpendicular to the background magnetic field. This temperature anisotropy is crucial in exciting and dissipating electromagnetic fluctuations in various plasma environments. Leveraging a comprehensive dataset comprising sub-ion scale measurements from NASA's Magnetospheric Multiscale Mission, our study unveils insights into the spatial evolution and parametric dependence of different ion kinetic instabilities within the Earth's magnetosheath. We observe a remarkable spatial dependence on the occurrence of kinetic instabilities. The condition for the mirror-mode instability exhibits a significantly higher prevalence near the subsolar magnetopause compared to the flank regions. The condition for the oblique firehose instability is more prominent near the bow shock region than in the vicinity of the magnetopause. Furthermore, the occurrence of these instabilities and their spatial distribution are linked to the plasma's upstream conditions. Our study offers new insights into the nature of ion kinetic instabilities in the Earth's magnetosheath and similar plasma environments.

Plain Language Summary Characterized by significantly compressed and heated solar wind, the Earth's magnetosheath is a region bounded by the bow shock and the Earth's magnetosphere, where plasma frequently exhibits unequal temperatures parallel and perpendicular to the background magnetic field. This temperature anisotropy excites electromagnetic fluctuations in various space and planetary plasma environments, which is often called plasma instabilities. However, it is still unclear how ion-kinetic instabilities evolve in the magnetosheath and their parametric dependence on upstream solar wind conditions. Using data from NASA's Magnetospheric Multiscale Mission, we find remarkable spatial and parametric dependence of ion-kinetic instabilities such as mirror-mode and firehose instabilities. Our result could be useful for understanding the nature of ion-kinetic instabilities in similar plasma environments.

1. Introduction

Downstream of the collisionless bow shock, the Earth's magnetosheath is a unique laboratory for studying plasma instabilities. These instabilities are prevalent in similar, yet inaccessible, astrophysical environments (e.g., in plasmas in which $T_p \gg T_e$, where T_i is the temperature of species i , and the subscripts p and e denote protons and electrons), such as the stellar corona and hot accretion flows. The supersonic solar wind undergoes sudden deceleration and compression across the bow shock, resulting in the formation of a highly dynamic magnetosheath characterized by locally generated turbulence and diverse instabilities (Fairfield, 1976; Guicking et al., 2012; Gurnett et al., 1979; Huang et al., 2017; Li et al., 2020; Schwartz et al., 1996). Previous research demonstrates the emergence of a power spectral density scaling of the magnetic-field fluctuations that follows approximately $\sim f^{-1}$ at the magnetohydrodynamic (MHD) scales in the magnetosheath, where f is the frequency in the spacecraft reference frame, indicating substantial local energy injection (Alexandrova et al., 2008; Chhiber et al., 2018; Czakowska et al., 2001; Huang et al., 2017; Li et al., 2020).

The presence of multiple wave types and instabilities is a common phenomenon downstream of shock transitions (Fairfield, 1976; Gurnett et al., 1979; Li et al., 2024; Lichko & Egedal, 2020; Rakhmanova et al., 2018; Rezeau et al., 1999; Sahraoui et al., 2006). Locally generated waves in the magnetosheath are correlated with pronounced temperature anisotropy of charged particles (e.g., $R_p = T_{p\perp}/T_{p\parallel} \neq 1$), where $T_{p\perp}$ ($T_{p\parallel}$) represents the temperature of protons perpendicular (parallel) to the background magnetic field (Anderson et al., 1994; Anderson & Fuselier, 1993; Dimmock et al., 2015; Lucek et al., 2001; Sahraoui et al., 2006; Schwartz et al., 1996; Song & Russell, 1997). Temperature anisotropy can drive various types of instabilities, including the Alfvén/ion-

cyclotron instability, the mirror-mode instability, the fast magnetosonic/whistler instability, and the fire-hose instability (Gary et al., 1998; Guicking et al., 2012; Hellinger & Matsumoto, 2000; Kunz et al., 2014; Ley et al., 2023; Quest & Shapiro, 1996; Southwood & Kivelson, 1993; Verscharen et al., 2016). Previous studies in both the solar wind and the magnetosheath indicate that most data point distributions in parameter space ($R_p, \beta_{p\parallel}$) are limited to the linear thresholds of kinetic instabilities (Bale et al., 2009; Kasper et al., 2008; Maruca et al., 2011, 2018), where $\beta_{p\parallel} = 2\mu_0 n_p k_B T_i / |B|^2$, μ_0 is the vacuum permeability, k_B is the Boltzmann constant, T_p the proton temperature, and $|B|$ is the magnetic field strength. However, a comprehensive investigation of the spatial distribution of the different types of ion kinetic instabilities and the influence of upstream solar wind conditions on this distribution is still lacking.

In the magnetosheath, plasma parameters such as magnetic field strength, plasma- β , and Alfvénic Mach number exhibit significant spatial variations. The most pronounced solar wind deceleration and compression occur in the sub-solar region downstream of the bow shock nose. As the magnetosheath plasma flows toward the flank regions, the plasma returns from subsonic to supersonic speeds (Li et al., 2020). The characteristics of field and plasma fluctuations evolve discernibly between the bow shock to the magnetopause, including the turbulent Mach number, intermittency, and the energy cascade rate (Jiang et al., 2022, 2024; Lewis et al., 2024; Li et al., 2020; Sahraoui et al., 2006; Yordanova et al., 2008). Instabilities and waves in the magnetosheath occur more frequently in close proximity to the bow shock (Guicking et al., 2012).

Variable upstream solar wind conditions and dynamic boundary conditions significantly alter the properties of the magnetosheath plasma. Under quasi-parallel shock conditions (i.e., with a small angle θ_{Bn} between the normal direction of the shock and the interplanetary magnetic field (IMF)), reflected field-aligned ion beams with $R_p < 1$ escape from the shock into the foreshock region where they generate intense and large-amplitude fluctuations through instability. These fluctuations are then convected with the plasma across the shock into the downstream magnetosheath (Dimmock et al., 2014; Lucek et al., 2008; Schwartz & Burgess, 1991; Soucek et al., 2008; Turc et al., 2023). In quasi-perpendicular shock scenarios, a prevalent temperature anisotropy ($R_p > 1$) exists in the magnetosheath (Dimmock et al., 2015; Sckopke et al., 1983; Soucek et al., 2015). Low-Mach shock conditions promote an increase in R_p , while mirror-mode fluctuations exhibit a higher occurrence rate behind low-Mach and quasi-perpendicular shocks (Soucek et al., 2015). Furthermore, under southward IMF conditions, magnetic field fluctuations near the magnetopause are significantly amplified (Dimmock et al., 2014). Higher upstream solar wind speeds are associated with a greater likelihood of high-amplitude fluctuations in the magnetosheath (Dimmock et al., 2014).

In this investigation, we leverage on the high-time resolution magnetic field and ion data obtained from NASA's *Magnetospheric Multiscale* Mission (MMS) to conduct a detailed analysis of kinetic instabilities in the Earth's magnetosheath. By utilizing a comprehensive dataset of MMS burst-mode events, we explore the parametric dependencies and spatial distribution of the occurrence of ion kinetic instabilities, examining their behavior under varying upstream solar wind conditions.

2. Data Set and Methods

2.1. Data Set

The high temporal resolution data provided by the MMS mission allow us to analyze plasma fluctuations, including variations in number density, bulk velocity, and temperature anisotropy, at sub-ion scales (Burch et al., 2016). The fluxgate magnetometer (FGM) records magnetic field data with a time resolution of 1/128 s (Russell et al., 2016), while the Fast Plasma Investigation (FPI) captures ion velocity distribution functions with a burst-mode time resolution of 0.15 s (Pollock et al., 2016). Our study involves a comprehensive statistical analysis of the thermodynamic properties and their correlations with ion-kinetic instabilities in magnetosheath plasma. We base our analysis on an event list that comprises 1,841 cases of burst-mode data collected by the MMS-1 spacecraft from September 2015 to June 2019 (Li et al., 2020).

2.2. Typical Unstable Events

Figure 1 illustrates unstable scenarios for the mirror-mode and oblique firehose instabilities in the dayside sub-solar region of the magnetosheath downstream of the bow shock on 25 January 2017 (left) and 06 October 2017

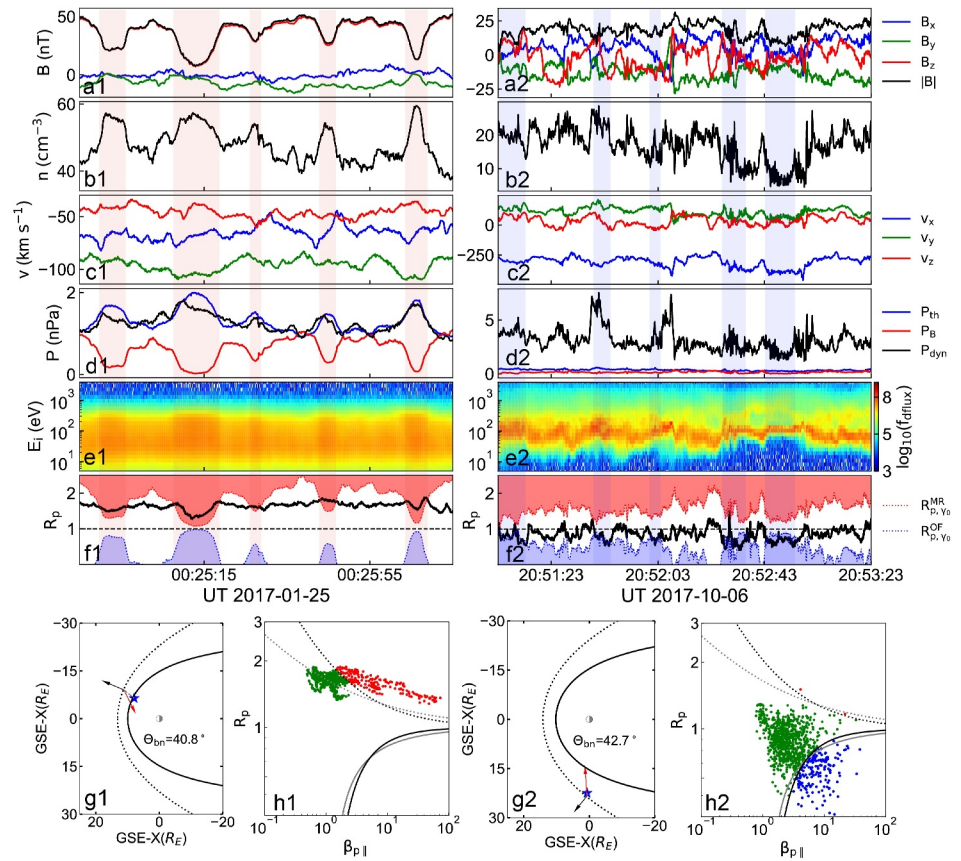


Figure 1. Mirror-mode and firehose instabilities observed by the MMS1 satellite on 25 January 2017 and 06 October 2017. (a) Magnetic field strength. (b) Ion number density. (c) Ion velocity in Geocentric Solar Ecliptic (GSE) coordinates. (d) Magnetic pressure, ion thermal pressure, and dynamic pressure. (e) Ion energy differential flux. (f) Ion temperature anisotropy and instability thresholds (indicated by dotted lines). The mirror-mode instability threshold is shown in red, and the oblique firehose instability threshold (with $\gamma = 10^{-2}\Omega_p$) is depicted in blue. (g) Average position of the spacecraft (marked by a blue star) and the angle between the shock normal and the IMF. The black and red arrows represent the projection of the IMF and the bow shock normal directions. (h) Distribution of R_p as a function of $\beta_{p\parallel}$. Unstable data points are highlighted in red (mirror-mode) and blue (oblique firehose). The black and gray dashed (solid) lines represent the thresholds for mirror-mode (oblique firehose) and Alfvén/ion-cyclotron (fast magnetosonic/whistler) instabilities when $\gamma = 10^{-2}\Omega_p$ (Verscharen et al., 2016).

(right). The average position of MMS1 lies between the bow shock (dotted line) and the magnetopause (solid line), determined using the dynamical bow shock and magnetopause models proposed by Shue et al. (1997) and Chao et al. (2002), which incorporate real-time upstream solar wind conditions from the OMNI data for position calculations (Papitashvili et al., 2014). Following a previous study by Li et al. (2020), we determine the geometry of the bow shock (θ_{Bn}) by calculating the angle between the IMF direction and the normal direction of the shock. To determine the normal direction of the shock, we radially project the average position of the spacecraft to the bow shock surface using a 3D empirical bow shock model (Chao et al., 2002) and calculate the normal vector at the projection point.

In the mirror-mode case, fluctuations in magnetic field strength and ion number density exhibit a clear anti-correlation, with local minima in magnetic field intensity at different times (light red shaded areas). These quasi-steady local minima, known as magnetic holes (Ahmadi et al., 2018; Breuillard et al., 2018; Jiang et al., 2022; Kitamura et al., 2020), are characterized by diamagnetic current and significant particle trapping (Haynes et al., 2015). The background plasma flow velocity is approximately 150 km/s, with dominant GSE-X and GSE-Y components of similar magnitudes, consistent with the expectations for magnetosheath plasma near the magnetopause. A local pressure balance is observed between plasma thermal pressure and magnetic pressure, with a small pressure gradient at the center of the magnetic holes where the magnetic field strength is minimal.

The average ion temperature is 190 eV, and R_p consistently exceeds 1. In certain regions within the magnetic holes, such as near 25:15 UT and 26:06 UT, localized reductions in R_p compared to the surroundings occur, possibly linked to adiabatic processes of ions within the weakened magnetic field regions of the holes (Ahmadi et al., 2018). The average R_p is 1.62, and the average $\beta_{p||}$ is 3.59.

In the case of the oblique firehose instability, the spacecraft is positioned near the bow shock transition region, as indicated in panel g2. The bow shock geometry is quasi-parallel, with an angle θ_{Bn} of approximately 42.7° . Significant fluctuations in both magnetic field strength and ion density are evident, with dynamic pressure exerting a dominant influence over magnetic and thermal pressures. The average value of R_p is 0.85, while the average $\beta_{p||}$ is 4.27.

2.3. Parametric Analysis of Unstable Plasma Conditions

To compare the growth rates of the mirror-mode and oblique firehose instabilities, we utilize fit relations based on linear Vlasov–Maxwell theory for four distinct types of ion kinetic instabilities driven by temperature anisotropy:

$$R_p^\gamma = 1 + \frac{a}{(\beta_{p||} - c)^b}, \quad (1)$$

where the parameters a , b , and c are different depending on the maximum growth rate γ for each instability. In this study, considering the typical plasma parameters observed in the magnetosheath, we use a , b , and c for a maximum growth rate $\gamma = 10^{-2}\Omega_p$. The parameters can be found in Table 1 of Verscharen et al. (2016).

Figures 1f1 and 1f2 depicts the values of R_p obtained from spacecraft observations (solid black line) alongside the mirror-mode (red dotted line) and oblique firehose instability (blue dotted line) thresholds R_p^γ calculated using the observed $\beta_{p||}$ with the parameters given by Table 1 in Verscharen et al. (2016). At the core of each magnetic hole, where the local minimum of the magnetic field magnitude is observed, R_p tends to surpass the mirror-mode instability threshold. This observation suggests that the mirror-mode instability prevalent in magnetosheath plasma often manifests itself within localized structures, displaying intermittent behavior over time and discrete spatial distribution. As the mirror-mode instability progresses, it triggers a gradual further reduction of the magnetic field strength, causing the magnetic hole structures to progressively steepen and deepen. Consequently, this leads to alterations in the dynamics and thermodynamic properties of ions and electrons (Jiang et al., 2022).

The onset of the oblique firehose instability appears to be linked with the rise in dynamic pressure near the bow shock. As illustrated in Figure 1h2, both the decrease in R_p and the increase in $\beta_{p||}$ contribute to the emergence of oblique firehose conditions. This effect is potentially also attributed to the presence of field-aligned ion beams observed near the quasi-parallel bow shock that contribute to higher $T_{p||}$ (Burgess & Scholer, 2013; Johlander et al., 2022; Liu et al., 2021; Preisser et al., 2020).

3. Statistical Results

3.1. Location Dependence of Ion-Kinetic Instabilities

To illustrate the statistical constraints imposed on magnetosheath plasma by kinetic instabilities, we present the probability density distribution of all our data points in the $R_p - \beta_{p||}$ plane in Figure 2a. The data points are organized in a 40×40 grid of logarithmically spaced bins covering the ranges $0.1 < \beta_{p||} < 100$ and $0.5 < R_p < 3$. The figure encompasses a total of 1,631,861 data points sampled at a time resolution of 0.15 s, with a notable concentration of high probability (75%) below the thresholds of the four kinetic instabilities (i.e., in the stable parameter regime). In Figure 2b, bins with data density below 0.005% are excluded, retaining 99% of the data points. This observation suggests that the majority of magnetosheath protons exhibit stability to these four types of ion kinetic instabilities. Nonetheless, a significant fraction of data points are considered unstable to kinetic instabilities due to proton temperature anisotropy surpassing the linear thresholds. This may be attributed to the high time resolution of the ion data compared to the time scale of the maximum linear growth rate $\gamma = 10^{-2}\Omega_p$ or to the driving of plasma turbulence, which pushes the plasma across the instability thresholds, being stronger than the relaxation by the instabilities.

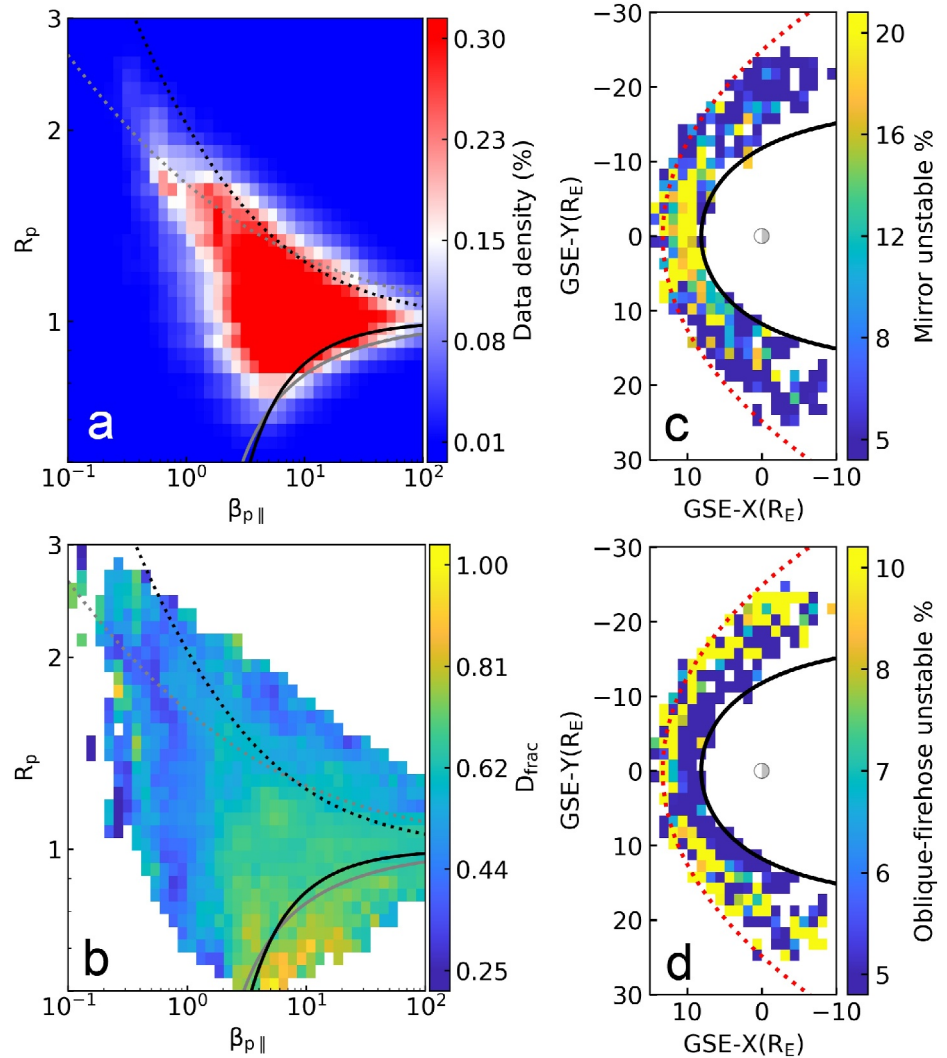


Figure 2. (a) The statistical probability distribution of data points in the $R_p - \beta_{p||}$ plane. (b) The statistical distribution of the spacecraft fractional distance (D_{frac}) to the magnetopause in the $R_p - \beta_{p||}$ plane. The black and gray dotted lines in both (a) and (b) represent the thresholds for the mirror-mode instability and the Alfvén/ion cyclotron wave instability when $\gamma = 10^{-2}\Omega_p$. Similarly, the black and gray solid lines represent the thresholds for the oblique-firehose and fast-magnetosonic/whistler instabilities. (c) and (d) The spatial distributions of cases unstable to mirror-mode and oblique-firehose instabilities as functions of the satellite position in the dayside equatorial GSE-XY plane.

The departure from the stable regime, as depicted in Figures 1e and 1g, predominantly occurs in coherent plasma structures such as magnetic holes, which can be generated by the mirror-mode instability (Jiang et al., 2022). This finding not only corroborates previous small-sample statistical analyses in the magnetosheath (Maruca et al., 2018) but also extends the conclusions drawn from studies in the solar wind at 1 au (Bale et al., 2009; Kasper et al., 2008; Maruca et al., 2011).

Compared with the Alfvén/ion cyclotron instability, the mirror-mode instability contour shows better alignment with the contour of the probability distribution of the data points in Figure 2a. This indicates that the mirror-mode threshold sets a slightly better $\beta_{p||}$ -dependent constraint to the proton temperature anisotropy (R_p) in the magnetosheath. Similarly, when $R_p < 1$, the magnetosheath plasma tends to approach the threshold curve of the fast magnetosonic/whistler and oblique firehose instabilities. Our result is consistent with observations in the solar wind reported in previous studies (Bale et al., 2009; Hellinger et al., 2006; Hellinger & Trávníček, 2014; Maruca et al., 2011, 2018). This may be due to the fact that oblique instabilities are non-propagating and more efficient in regulating the temperature anisotropy as shown by previous numerical and observational studies in slow solar

wind (Hellinger et al., 2006; Hellinger & Matsumoto, 2001). An alternative explanation for the plasma's neglect for the Alfvén/ion cyclotron instability threshold lies in the strong dependence of resonant instabilities on local velocity-space gradients, creating uncertainty in their threshold values (Walters et al., 2023). The mirror-mode instability is less sensitive to the exact shape of these gradients, so that the predicted mirror-mode threshold is more accurate even in plasmas that deviate from the bi-Maxwellian model assumption.

To study the spatial dependence of the ion thermodynamic properties in the magnetosheath, we use the fractional distance between the spacecraft and the magnetopause (D_{frac}) as proposed by Verigin et al. (2006):

$$D_{\text{frac}} = \frac{r_{\text{sc}} - r_{\text{mp}}}{r_{\text{bs}} - r_{\text{mp}}}, \quad (2)$$

where r_{sc} , r_{mp} and r_{bs} are the radial distances of the spacecraft, the Earth's magnetopause and the bow shock away from the Earth center. r_{sc} is obtained from the MMS-1 orbital data, and r_{mp} and r_{bs} are derived from the dynamical bow shock and magnetopause empirical models (Chao et al., 2002; Shue et al., 1997) with upstream solar wind parameters from OMNI data as input.

Figure 2b illustrates the spacecraft distance D_{frac} relative to the magnetopause for all data points in the $R_p - \beta_{\text{p||}}$ parameter plane. The color represents the average D_{frac} within each bin. A value of D_{frac} close to 1 indicates proximity to the bow shock, while a value close to 0 signifies proximity to the magnetopause. In Figure 2b, data in the unstable regime to the oblique firehose and FM/W instability have a higher average $D_{\text{frac}} \approx 1$ than in other parts of parameter space. In contrast, data points in proximity to the mirror-mode instability and the Alfvén/ion cyclotron instability have smaller average D_{frac} values, indicating closer proximity to the magnetopause and a higher likelihood of instability with $R_p > 1$.

Figures 2c and 2d depict the spatial distribution of the percentage of unstable data points for the two non-propagating ion kinetic instabilities (i.e., surpassing the thresholds of the mirror-mode and oblique-firehose instabilities) in the equatorial GSE-XY plane. Data points are organized into a 20×40 grid of linearly spaced bins that cover the ranges $-10 < X_{\text{GSE}}/R_E < 15$ and $-30 < Y_{\text{GSE}}/R_E < 30$, where R_E is the radius of Earth. The dotted red and solid black lines denote the nominal positions of the bow shock and magnetopause. We observe distinct spatial patterns for the mirror-mode instability and the oblique-firehose instability in the magnetosheath. Consistent with the D_{frac} findings, the mirror-mode instability is more prevalent in the subsolar region compared to the flank region (see Figure 2c). In contrast, the oblique-firehose instability exhibits a clear radial dependence from the bow shock toward the magnetopause, with the percentage of unstable data points decreasing with radial distance from Earth.

3.2. Dependence on Upstream Solar Wind Conditions

Given the direct impact of varying upstream solar wind parameters and interplanetary magnetic field configurations on R_p and $\beta_{\text{p||}}$ in the magnetosheath downstream of the bow shock, we perform a statistical analysis of the correlation of ion kinetic instabilities with different upstream solar wind conditions. We use the interplanetary magnetic field (IMF) and plasma data sourced from OMNI in the upstream solar wind. These data enable us to evaluate factors such as the spacecraft's relative spatial position to the magnetopause, the geometry of the upstream bow shock (θ_{Bn}), dynamic pressure ($P_{\text{dyn,sw}}$), magnetosonic Mach number ($M_{\text{ms,sw}}$), and the Z-component of the IMF (B_z).

Figure 3 shows the real-time distribution of upstream parameters that correspond to the magnetosheath data points in $R_p - \beta_{\text{p||}}$ parameter space. As depicted in Figure 3a, we observe that a quasi-perpendicular bow shock geometry (i.e., $\theta_{\text{Bn}} > 60^\circ$) tends to favor the Alfvén/ion cyclotron and mirror-mode instabilities, while quasi-parallel conditions (i.e., $\theta_{\text{Bn}} < 30^\circ$) are conducive to the fast-magnetosonic/whistler-wave and oblique-firehose instabilities. Elevated solar wind dynamic pressure increases the likelihood of triggering the Alfvén/ion-cyclotron instability. Moreover, for relatively high values of $M_{\text{ms,sw}}$, both the mirror-mode instability and the oblique-firehose instability are more likely to occur. Specifically, under conditions of high $M_{\text{ms,sw}}$ (> 7.1), the magnetosheath plasma exhibits a higher susceptibility to mirror mode instability, which aligns with previous findings (Soucek et al., 2015). However, we do not observe a clear statistical dependence on the IMF B_z value.

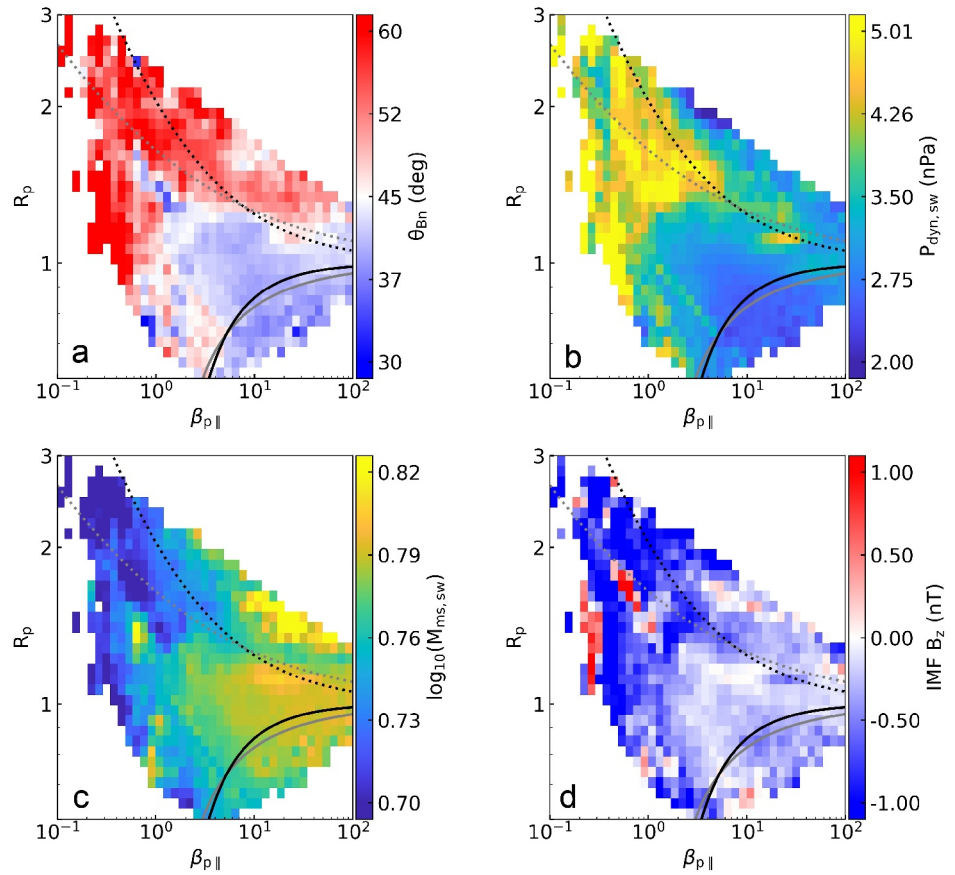


Figure 3. The statistical distributions of upstream conditions computed from OMNI data corresponding to each data point in the $R_p - \beta_{p||}$ plane. (a) The bow shock normal angle θ_{Bn} calculated using upstream interplanetary magnetic field. (b) The upstream solar wind dynamic pressure $P_{\text{dyn,sw}}$. (c) The upstream solar wind magnetosonic Mach number $M_{\text{ms,sw}}$. (d) Z-component of the upstream interplanetary magnetic field B_z . The overplotted curves are defined as in Figure 2.

Figures 4a1 and 4a2 illustrate the statistical distributions of D_{frac} for data points downstream of a bow shock configuration with $\theta_{Bn} > 60^\circ$ (quasi-perpendicular) and $\theta_{Bn} < 30^\circ$ (quasi-parallel). In the case of quasi-parallel shock configurations, a significant number of data near the bow shock are biased toward $R_p < 1$. Downstream of quasi-perpendicular shock geometries, there is a similar but weak pattern in the data distribution regarding the D_{frac} dependence. As shown in Figure 4a3, we find a similar pattern when quantifying the occurrence rates of plasma conditions unstable to the mirror-mode and the oblique-firehose instabilities as a function of D_{frac} using divided data sets according to different upstream parameters. However, when using thresholds with a smaller growth rate $\gamma = 10^{-3}\Omega_p$, the unstable plasma conditions also significantly dependent on D_{frac} .

To ensure robust statistical analysis, we partition the dataset based on the median values of each parameter, including the upstream solar wind dynamic pressure, fast magnetosonic Mach number, and IMF B_z . Figures 4b1 and 4b2 compare the statistical distribution of D_{frac} conditioned for low and high solar wind dynamic pressures. The observed trend aligns closely with that in Figure 4a2. However, in the presence of high dynamic pressure, we find that the oblique firehose instability more likely to occur near the bow shock, as illustrated in Figure 4f. This feature persists when using thresholds with a smaller maximum growth rate $\gamma = 10^{-3}\Omega_p$ as shown in Figure 4b3. Figures 4c1 and 4c2 reveal a notable disparity when the data set is conditioned for high or low $M_{\text{ms,sw}}$. When $M_{\text{ms,sw}} > 6$, the location dependence is pronounced, and regions near the bow shock predominantly show data above the thresholds for the $R_p < 1$ instabilities (Figure 4f). Conversely, for $M_{\text{ms,sw}} < 6$, the location dependence weakens, and the average D_{frac} converges toward 0.5. This locational dependence is weakened when using thresholds with a smaller maximum growth rate as shown in Figure 4c3.

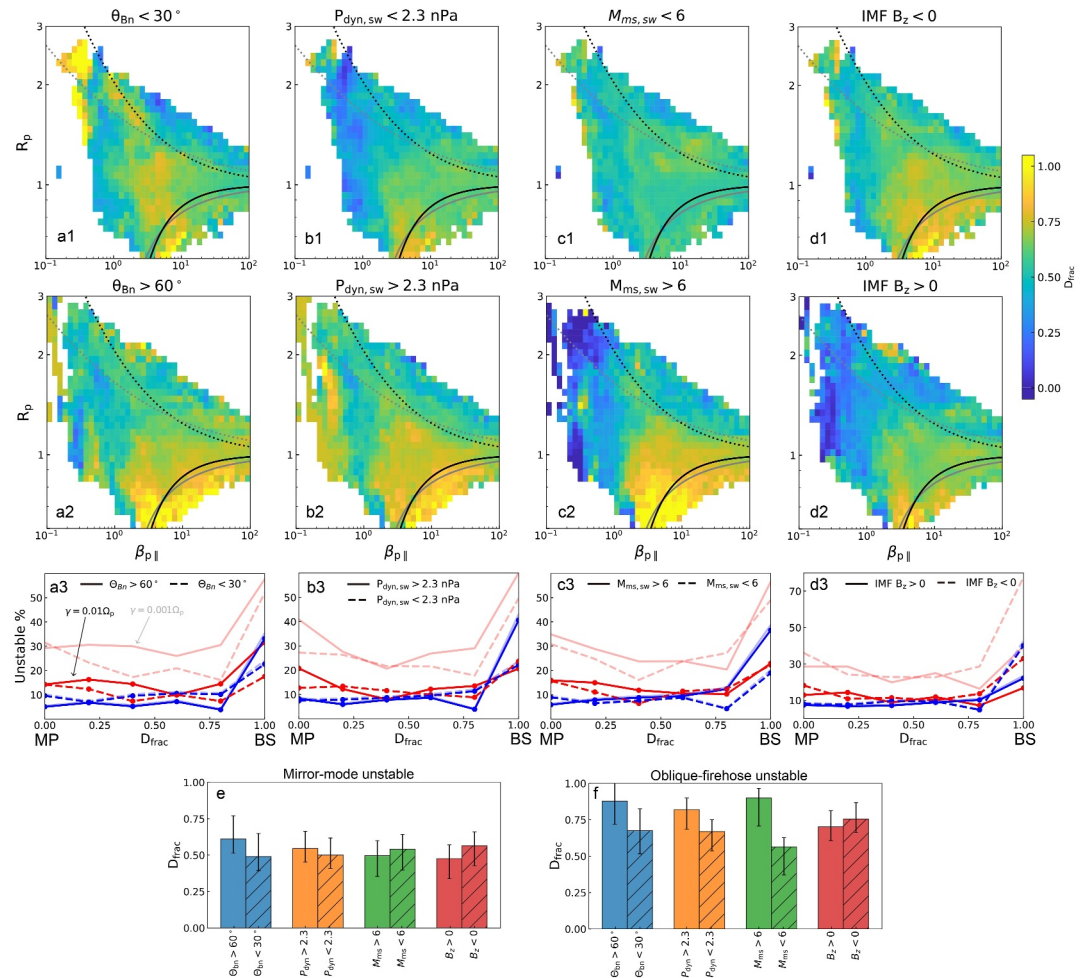


Figure 4. Statistical distributions of the spacecraft fractional distance D_{frac} to the magnetopause under different upstream conditions in the $R_p - \beta_{p||}$ plane. The statistical distributions of D_{frac} under quasi-parallel (a1) and quasi-perpendicular (a2) bow shock geometries and, under small (b1) and great (b2) solar wind dynamic pressures, under small (c1) and large (c2) solar wind magnetosonic Mach numbers, and under south (d1) and north (d2) IMF conditions. (a3–d3) Occurrence rates of unstable plasma conditions for the mirror-mode (red) and the oblique-firehose (blue) instabilities as a function of D_{frac} . Light-colored lines represent results of different thresholds with the growth rate $\gamma = 10^{-3}\Omega_p$. The average D_{frac} of categorized datasets for mirror-mode unstable conditions (e) and oblique-firehose unstable conditions (f). The error bars represent the standard error of mean values.

Figures 4d1 and 4d2 present the statistical distributions of D_{frac} in the magnetosheath under conditions of southward IMF ($B_z < 0$) and northward IMF ($B_z > 0$). For $B_z > 0$, the data points above the mirror-mode threshold exhibit smaller D_{frac} (< 0.5). In contrast, under $B_z < 0$, those firehose-unstable intervals have a slightly higher D_{frac} (> 0.8), suggesting that they are more likely to be observed near the shock. In regions near the bow shock ($D_{\text{frac}} > 0.8$), the proportion of unstable firehose data points approaches 30%, exceeding the values observed in other regions, as indicated by Figure 4f. For results with a smaller growth rate as shown in Figure 4d3, we find a similar and more significant dependence during the southward IMF condition.

Figure 5 shows the distribution of the local time of data points in the $R_p - \beta_{p||}$ plane. The local time is defined as $12(\pi + \arctan(Y_{\text{GSE}}/X_{\text{GSE}}))/\pi$. A local time close to 12 means that the measurement position is close to the dayside subsolar region of the magnetosheath. A local time of about 6 or 18 indicates that the data points in the magnetosheath are recorded close to the dawnside or duskside of the flank region. When $\theta_{\text{Bn}} < 30^\circ$ (quasi-parallel), a notable portion of data points unstable to the Alfvén/ion cyclotron instability with $\beta_{p||} \approx 1$ are observed at the dusk side. In contrast, for the $\theta_{\text{Bn}} > 60^\circ$ (quasi-perpendicular) scenario, the dawn-dusk asymmetry is less pronounced,

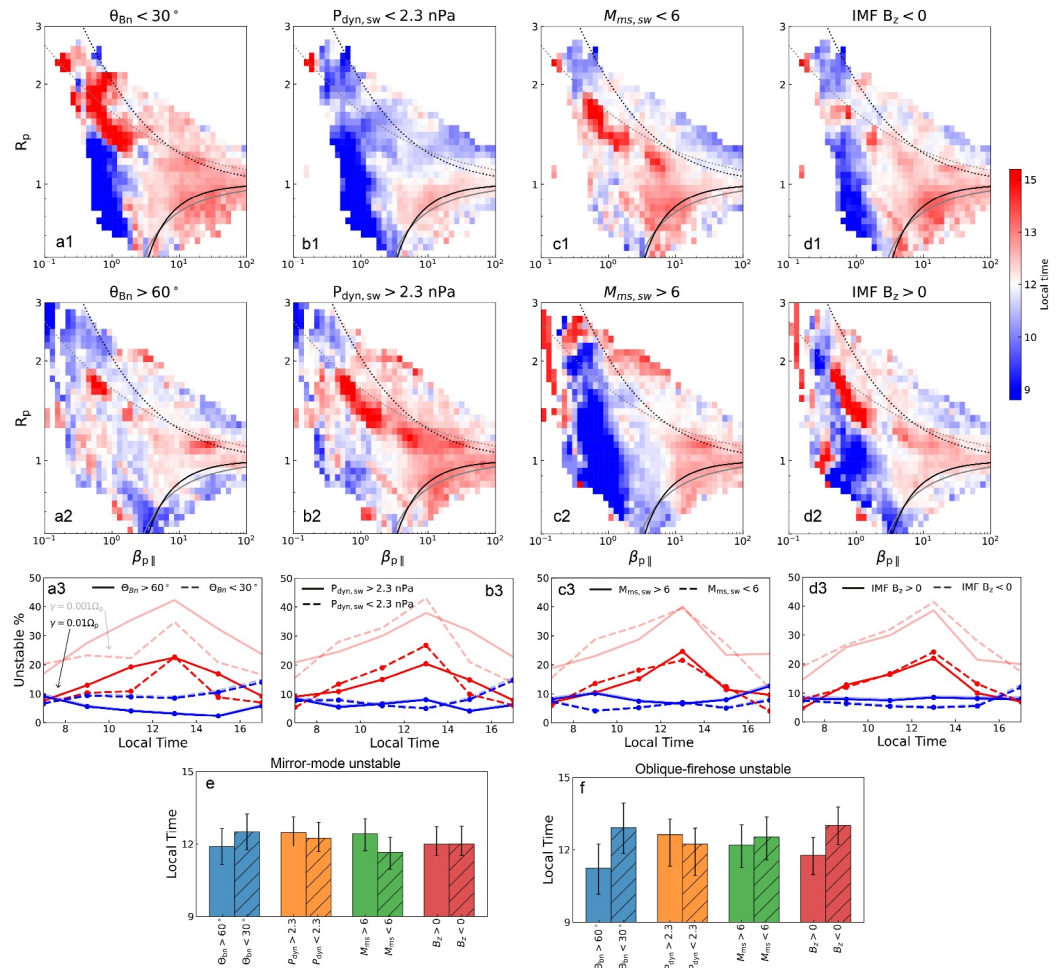


Figure 5. Statistical distributions of the spacecraft local time under different upstream conditions in the $R_p - \beta_{p||}$ plane. The statistical distributions of the local time under quasi-parallel (a1) and quasi-perpendicular (a2) bow shock geometries and under small (b1) and great (b2) solar wind dynamic pressures, under small (c1) and large (c2) solar wind magnetosonic Mach numbers, and under south (d1) and north (d2) IMF conditions. (a3–d3) Occurrence rates of unstable plasma conditions for the mirror-mode (red) and the oblique-firehose (blue) instabilities as a function of the local time. Light-colored lines represent results of different thresholds with the growth rate $\gamma = 10^{-3}\Omega_p$. The average local time of categorized datasets for mirror-mode unstable conditions (e) and oblique-firehose unstable conditions (f). The error bars represent the standard error of mean values.

with a slight intensification near the Alfvén/ion cyclotron instability contour on the duskside. For the oblique-firehose instability, the local-time dependence of unstable conditions shows opposite trends in Figure 5a3.

When the dynamic pressure $P_{\text{dyn,sw}} > 2.3$ nPa, data points unstable to the Alfvén/ion cyclotron instability and firehose instabilities are observed at the dusk side, as depicted in Figure 5b2. When $P_{\text{dyn,sw}} < 2.3$ nPa, the duskside and regions near the subsolar area are slightly prone to firehose instabilities as shown in Figures 5b1 and 5b3. For $M_{\text{ms,sw}} > 6$, the data points unstable to firehose instabilities are slightly more likely to be present at the dusk flank side with $\beta_{p||} > 10$. Regardless of the sign of B_z , the plasma conditions unstable to the oblique-firehose instability show no significant dependence on the local time. For all data points, as depicted in Figures 5a3–5d3, the mirror-mode instability exhibits a distinct dawn-dusk asymmetry, with a higher percentage of unstable data points observed on the dusk side. For results with a smaller maximum growth rate, we find a very similar dawn-dusk asymmetry for the mirror-mode instability regardless of the upstream conditions.

4. Discussion and Conclusions

Utilizing the high time-resolution ion data obtained from the Magnetospheric Multiscale (MMS) Mission, we conduct an extensive statistical analysis of the spatial distribution of ion kinetic instabilities in the Earth's magnetosheath. This study is based on a comprehensive list of burst-mode events that cover the dayside magnetosheath between September 2015 and June 2019 (Li et al., 2020). By combining predictions for the thresholds of four anisotropy-driven instabilities from linear Vlasov–Maxwell theory with sub-ion scale measurements of ion parameters, we evaluate the stability of plasma in different regions of the magnetosheath and depending on upstream plasma conditions. The four instabilities are the mirror-mode instability, Alfvén/ion cyclotron instability, oblique firehose instability, and fast magnetosonic/whistler instability.

Our findings reveal a notable spatial dependence in the occurrence rates of data that exceed the thresholds for the four kinetic instabilities. Among the total 1,631,861 data points analyzed, around 25% of the whole data exceed the instability thresholds; that is, are located in the unstable region of parameter space. The occurrence rate of the mirror-mode instability exhibits its maximum (>20%) in spatial bins in the subsolar region of the magnetosheath, with a gradual decrease as the plasma flows toward the flank regions. In contrast, the occurrence rate of the oblique-firehose instability shows its maximum (>10%) in spatial bins near the bow shock, decreasing significantly with radial distance to the magnetopause.

To quantify the radial dependence, we apply a dimensionless fractional distance D_{frac} to the magnetopause based on dynamic bow shock and magnetopause models that use real-time solar wind parameters from OMNI data. Our analysis confirms that the distribution of D_{frac} near the firehose instability threshold is >0.8 (proximity to the bow shock), gradually decreasing with increasing R_p . Near the mirror-mode instability threshold, the average D_{frac} decreases to values indicating vicinity to the magnetopause on average. The occurrence rate of the mirror-mode instability is greatest near the bow shock (25%), which is consistent with previous study (Soucek et al., 2015). However, we show that the occurrence rate of the mirror-mode instability are higher near the magnetopause (18%) than in the central magnetosheath (10%).

The occurrence of unstable conditions for ion kinetic instabilities shows distinct dependencies on the upstream solar wind conditions in terms of its location and local time in the magnetosheath. Quasi-perpendicular bow shock geometry favors the Alfvén/ion cyclotron and mirror-mode instabilities, while the fast-magnetosonic/whistler and oblique-firehose instabilities are more prevalent under quasi-parallel shock conditions. High solar wind dynamic pressure ($P_{\text{dyn,sw}} > 5$ nPa) promotes the occurrence of Alfvén/ion cyclotron instability in the dusk magnetosheath, with a dawn-dusk asymmetry in fast-magnetosonic/whistler and oblique-firehose instabilities based on the sign of the IMF B_z . The radial dependence of the oblique-firehose instability is more pronounced when the upstream fast magnetosonic Mach number and dynamic pressure are large. In contrast, the mirror-mode instability does not show significant dependence on the radial distance or local time across our conditioned subsets of data using upstream parameters.

This study focuses on plasma conditions for ion kinetic instabilities that generate electromagnetic fluctuations at ion kinetic scales, for example, mirror-mode waves, proton cyclotron waves and low-frequency whistler waves. These waves exhibit distinct frequencies and polarizations in their magnetic-field fluctuations. To investigate potential unstable plasma conditions predicted by the linear Vlasov-Maxwell theory and their relationship with observable wave activity in the magnetosheath, we conduct a statistical analysis on the polarization properties of magnetic-field fluctuations. By applying the singular value decomposition method (Santolík et al., 2003), we present an example with strong wave activity and the polarization properties such as the ellipticity, the planarity, and the degree of polarization (DOP) of the magnetic-field fluctuations in Figures 6a–6g. Concurrent with plasma conditions unstable to mirror-mode instability, this example shows strong signatures of coherent wave activity at frequencies near 0.2 Hz in the spacecraft frame. For each time stamp, the polarization parameters (with DOP >0.7 and planarity >0.7) near ion cyclotron frequencies with the strongest power spectral density (PSD) of the magnetic-field fluctuations are shown in Figure 6g and used in our statistical analysis in Figures 6h–6k.

The wave characteristics depicted in Figures 6a–6g align with mirror-mode waves, which are linearly polarized (with minimal ellipticity near 0) in the magnetic-field fluctuations and obliquely propagating relative to the background magnetic field direction (usually between 70 and 80°, not shown here). By mapping the polarization parameters, including ellipticity and power spectral density (PSD) of magnetic-field fluctuations at the corresponding frequency in the $R_p - \beta_{\text{p||}}$ plane for both the example case and the statistical dataset, Figures 6h and 6i

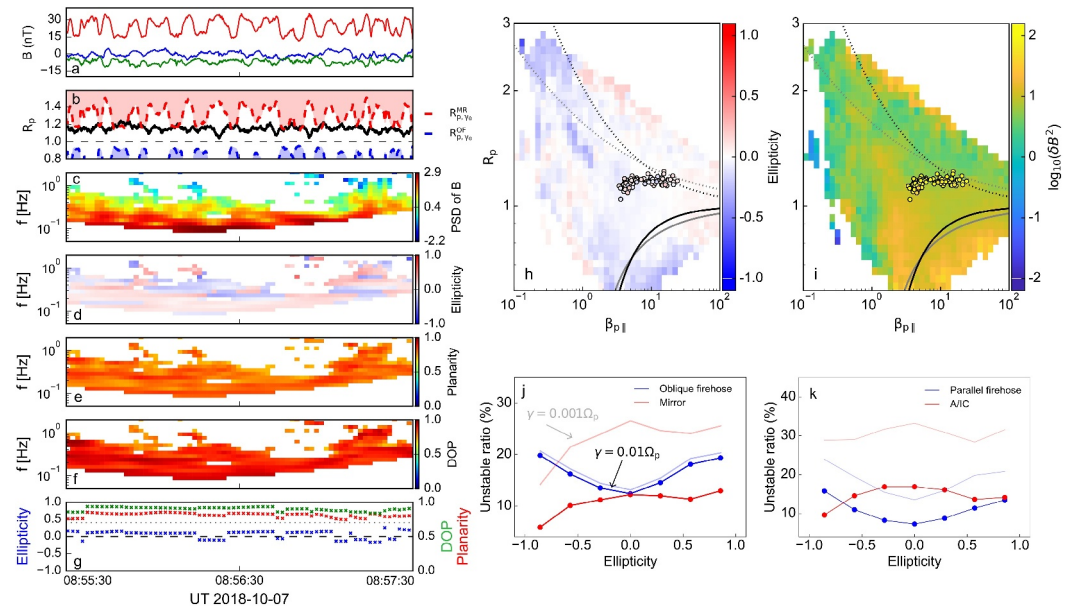


Figure 6. Polarization analysis of an example with strong mirror-mode wave activity observed by the MMS satellite on 07 October 2018. (a) Magnetic field. (b) Ion temperature anisotropy and instability thresholds (indicated by dotted lines). (c) Power spectral density (PSD) of the magnetic-field fluctuations. (d) Ellipticity. (e) Planarity. (f) Degree of polarization (DOP). (g) Polarization parameters at the frequency with the maximum PSD. Statistical results of the polarization parameters in the magnetosheath. (h) and (i) Ellipticity and PSD of the magnetic-field fluctuations mapped in the $R_p - \beta_{p||}$ plane. The colored circles represent the data points of the wave example. The format is the same as Figures. (j) and (k) Occurrence rates of plasma conditions unstable to four different instabilities as a function of the ellipticity. Light-colored lines represent results of different thresholds with the growth rate $\gamma = 10^{-3}\Omega_p$.

show the statistical distributions of the polarization parameters. For parameters close to the mirror-mode instability contour, the average ellipticity of magnetic-field fluctuations is small and close to zero, particularly around $\beta_{p||} \approx 10$, consistent with mirror-mode instability predictions. We also find left-handed circularly polarized waves in regions with low $\beta_{p||}$ values ($\beta_{p||} < 1$) and significant temperature anisotropy ($R_p \geq 1.4$) near the Alfvén/ion cyclotron instability threshold. These left-handed polarized waves exhibit enhanced wave power in the parameter space near or below the thresholds of the fast magnetosonic/whistler instability or oblique firehose instability. Additionally, right-handed polarized waves are present in regions with relatively high $\beta_{p||}$ (>20). However, this statistical mapping method limits further interpretation by not providing a point-wise correlation between different wave modes and the prediction of growth rates for corresponding instabilities based on local plasma conditions (McManus et al., 2024). Dividing the ellipticity dataset into 7 bins, we calculate the occurrence rates of plasma conditions unstable to the four types of instabilities with growth rates $\gamma = 10^{-2}\Omega_p$ and $\gamma = 10^{-3}\Omega_p$ in each subset. We observe higher occurrence rates of plasma conditions unstable to mirror-mode instability in regions with low ellipticity, especially at $\gamma = 10^{-3}\Omega_p$. The occurrence ratio of mirror-mode instability slightly increases as ellipticity approaches ≈ 0.8 .

For left-handed polarizations, the occurrence rate of conditions unstable to Alfvén/ion cyclotron instability in Figure 6k increases from 10% to $\approx 30\%$ (compared to $\approx 25\%$ for mirror-mode instability) when transitioning growth rate thresholds from $\gamma = 10^{-2}\Omega_p$ to $\gamma = 10^{-3}\Omega_p$ at ellipticity < -0.5 . Higher occurrence rates of unstable plasma conditions with more circular polarizations (greater absolute values of ellipticity) in magnetic-field fluctuations are observed for both parallel and oblique firehose instabilities. This finding is partially consistent with previous observations and predictions regarding the fast magnetosonic/whistler instability driving right-handed circularly polarized waves (Gary et al., 2016; Klein et al., 2019, 2021; McManus et al., 2024; Verscharen et al., 2019). However, the Doppler effect may alter the sign of ellipticity of these circularly polarized waves observed in the spacecraft frame (Jian et al., 2010). A comprehensive statistical analysis of the Doppler shift effect in the magnetosheath is required for future investigations.

Furthermore, it is important to acknowledge the limitations of our current analysis stemming from the assumption of bi-Maxwellian ion VDFs in the linear Vlasov-Maxwell theory. The exploration of non-Maxwellian VDFs falls outside the scope of our present study. The presence of proton beams, as well as heavy ions, is neglected because of the lack of data in the MMS/FPI/DIS moments dataset. It is worth noting that previous research (Perri et al., 2020) has highlighted the frequent observation of non-Maxwellian ion VDFs in the magnetosheath. The variability in ion VDFs downstream quasi-parallel bow shock underscores the complex nature of interactions in the turbulent magnetosheath. Future studies should consider the extent of non-Maxwellian VDFs and specific velocity-space structures like beams (Walters et al., 2023; Woodham et al., 2019) for a more comprehensive understanding.

Data Availability Statement

The MMS data are available through the MMS Science Data Center <https://lasp.colorado.edu/mms/sdc/public/>, and the CDA Web <https://cdaweb.gsfc.nasa.gov/>. The OMNI data are available from the GSFC/SPDF OMNIWeb interface <https://omniweb.gsfc.nasa.gov>.

Acknowledgments

The authors thank the MMS team for the FGM and FPI data (<https://lasp.colorado.edu/mms/sdc/public>) and NASA CDAWEB for the OMNI data (<https://cdaweb.sci.gsfc.nasa.gov/index.html/>). This work is supported by the NNSFC grants (Grant 42374198, 42188101, 42404177, 42274210), project of Civil Aerospace “fourteenth Five Year Plan” Preliminary Research in Space Science (D010302, D010202) and National Key Research and Development Program of China (No. 2021YFA0718600). W.J. is supported by NSSC Youth grant and the Specialized Research Fund for State Key Laboratories of China. H. Li is supported by the International Partnership Program of CAS (Grant 183311KYSB20200017). D.V. is supported by STFC Consolidated Grant ST/W001004/1.

References

- Ahmadi, N., Wilder, F. D., Ergun, R. E., Argall, M., Usanova, M. E., Breuillard, H., et al. (2018). Generation of electron whistler waves at the mirror mode magnetic holes: MMS observations and PIC simulation. *Journal of Geophysical Research: Space Physics*, *123*(8), 6383–6393. <https://doi.org/10.1029/2018JA025452>
- Alexandrova, O., Lacombe, C., & Mangeney, A. (2008). Spectra and anisotropy of magnetic fluctuations in the Earth’s magnetosheath: Cluster observations. *Annales Geophysicae*, *26*(11), 3585–3596. <https://doi.org/10.5194/angeo-26-3585-2008>
- Anderson, B. J., & Fuselier, S. A. (1993). Magnetic pulsations from 0.1 to 4.0 Hz and associated plasma properties in the Earth’s subsolar magnetosheath and plasma depletion layer. *Journal of Geophysical Research: Space Physics*, *98*(A2), 1461–1479. <https://doi.org/10.1029/92JA02197>
- Anderson, B. J., Fuselier, S. A., Gary, S. P., & Denton, R. E. (1994). Magnetic spectral signatures in the Earth’s magnetosheath and plasma depletion layer. *Journal of Geophysical Research*, *99*(A4), 5877–5891. <https://doi.org/10.1029/93JA02827>
- Bale, S. D., Kasper, J. C., Howes, G. G., Quataert, E., Salem, C., & Sundkvist, D. (2009). Magnetic fluctuation power near proton temperature anisotropy instability thresholds in the solar wind. *Physical Review Letters*, *103*(21), 211101. <https://doi.org/10.1103/PhysRevLett.103.211101>
- Breuillard, H., Le Contel, O., Chust, T., Berthomier, M., Retino, A., Turner, D. L., et al. (2018). The properties of lion roars and electron dynamics in mirror mode waves observed by the magnetospheric MultiScale mission. *JGR Space Physics*, *123*(1), 93–103. <https://doi.org/10.1002/2017JA024551>
- Burch, J. L., Moore, T. E., Torbert, R. B., & Giles, B. L. (2016). Magnetospheric Multiscale overview and science objectives. *Space Science Reviews*, *199*(1–4), 5–21. <https://doi.org/10.1007/s11214-015-0164-9>
- Burgess, D., & Scholer, M. (2013). Microphysics of quasi-parallel shocks in collisionless plasmas. *Space Science Reviews*, *178*(2), 513–533. <https://doi.org/10.1007/s11214-013-9969-6>
- Chao, J., Wu, D., Lin, C.-H., Yang, Y.-H., Wang, X., Kessel, M., et al. (2002). Models for the size and shape of the earth’s magnetopause and bow shock. Vol. 12. In *COSPAR colloquia series* (pp. 127–135). Elsevier. [https://doi.org/10.1016/S0964-2749\(02\)80212-8](https://doi.org/10.1016/S0964-2749(02)80212-8)
- Chhiber, R., Chasapis, A., Bandyopadhyay, R., Parashar, T. N., Matthaeus, W. H., Maruca, B. A., et al. (2018). Higher-order turbulence statistics in the earth’s magnetosheath and the solar wind using magnetospheric Multiscale observations. *Journal of Geophysical Research: Space Physics*, *123*(12), 9941–9954. <https://doi.org/10.1029/2018JA025768>
- Czaykowska, A., Bauer, T. M., Treumann, R. A., & Baumjohann, W. (2001). Magnetic field fluctuations across the Earth’s bow shock. *Annales Geophysicae*, *19*(3), 275–287. <https://doi.org/10.5194/angeo-19-275-2001>
- Dimmock, A. P., Nykyri, K., & Pulkkinen, T. I. (2014). A statistical study of magnetic field fluctuations in the dayside magnetosheath and their dependence on upstream solar wind conditions. *Journal of Geophysical Research: Space Physics*, *119*(8), 6231–6248. <https://doi.org/10.1002/2014JA020009>
- Dimmock, A. P., Osmane, A., Pulkkinen, T. I., & Nykyri, K. (2015). A statistical study of the dawn-dusk asymmetry of ion temperature anisotropy and mirror mode occurrence in the terrestrial dayside magnetosheath using THEMIS data. *Journal of Geophysical Research: Space Physics*, *120*(7), 5489–5503. <https://doi.org/10.1002/2015JA021192>
- Fairfield, D. H. (1976). Magnetic fields of the magnetosheath. *Reviews of Geophysics*, *14*(1), 117–134. <https://doi.org/10.1029/RG014i001p00117>
- Gary, S. P., Jian, L. K., Broiles, T. W., Stevens, M. L., Podesta, J. J., & Kasper, J. C. (2016). Ion-driven instabilities in the solar wind: Wind observations of 19 March 2005. *JGR Space Physics*, *121*(1), 30–41. <https://doi.org/10.1002/2015JA021935>
- Gary, S. P., Li, H., O’Rourke, S., & Winske, D. (1998). Proton resonant firehose instability: Temperature anisotropy and fluctuating field constraints. *Journal of Geophysical Research*, *103*(A7), 14567–14574. <https://doi.org/10.1029/98JA01174>
- Guicking, L., Glassmeier, K.-H., Auster, H.-U., Narita, Y., & Kleindienst, G. (2012). Low-frequency magnetic field fluctuations in Earth’s plasma environment observed by THEMIS. *Annales Geophysicae*, *30*(8), 1271–1283. <https://doi.org/10.5194/angeo-30-1271-2012>
- Gurnett, D., Anderson, R., Tsurutani, B., Smith, E., Paschmann, G., Haerendel, G., et al. (1979). Plasma-wave turbulence at the magnetopause - Observations from isee 1 and 2. *Journal of Geophysical Research-Space Physics*, *84*(NA12), 7043–7058. <https://doi.org/10.1029/JA084iA12p07043>
- Haynes, C. T., Burgess, D., Camporeale, E., & Sundberg, T. (2015). Electron vortex magnetic holes: A nonlinear coherent plasma structure. *Physics of Plasmas*, *22*(1), 012309. <https://doi.org/10.1063/1.4906356>
- Hellinger, P., & Matsumoto, H. (2000). New kinetic instability: Oblique Alfvén fire hose. *Journal of Geophysical Research*, *105*(A5), 10519–10526. <https://doi.org/10.1029/1999JA000297>
- Hellinger, P., & Matsumoto, H. (2001). Nonlinear competition between the whistler and Alfvén fire hoses. *Journal of Geophysical Research*, *106*(A7), 13215–13218. <https://doi.org/10.1029/2001JA900026>

- Hellinger, P., Trávníček, P., Kasper, J. C., & Lazarus, A. J. (2006). Solar wind proton temperature anisotropy: Linear theory and WIND/SWE observations. *Geophysical Research Letters*, *33*(9), 2006GL025925. <https://doi.org/10.1029/2006GL025925>
- Hellinger, P., & Trávníček, P. M. (2014). Solar wind protons at 1 au: Trends and bounds, constraints and correlations. *Acta Pathologica Japonica*, *78*(1), L15. <https://doi.org/10.1088/2041-8205/78/1/L15>
- Huang, S. Y., Hadid, L. Z., Sahraoui, F., Yuan, Z. G., & Deng, X. H. (2017). On the existence of the Kolmogorov inertial range in the terrestrial magnetosheath turbulence. *The Astrophysical Journal*, *836*(1), L10. <https://doi.org/10.3847/2041-8213/836/1/L10>
- Jian, L. K., Russell, C. T., Luhmann, J. G., Anderson, B. J., Boardsen, S. A., Strangeway, R. J., et al. (2010). Observations of ion cyclotron waves in the solar wind near 0.3 au: Observations of ICWs near 0.3 au. *Journal of Geophysical Research*, *115*(A12). <https://doi.org/10.1029/2010JA015737>
- Jiang, W., Verscharen, D., Jeong, S.-Y., Li, H., Klein, K. G., Owen, C. J., & Wang, C. (2024). Velocity-space signatures of resonant energy transfer between whistler waves and electrons in the earth's magnetosheath. *ApJ*, *960*(1), 30. <https://doi.org/10.3847/1538-4357/ad0df8>
- Jiang, W., Verscharen, D., Li, H., Wang, C., & Klein, K. G. (2022). Whistler waves as a signature of converging magnetic holes in space plasmas. *ApJ*, *935*(2), 169. <https://doi.org/10.3847/1538-4357/ac7ce2>
- Johlander, A., Battarbee, M., Turc, L., Ganse, U., Pfau-Kempf, Y., Grandin, M., et al. (2022). Quasi-parallel shock reformation seen by magnetospheric Multiscale and ion-kinetic simulations. *Geophysical Research Letters*, *49*(2), e2021GL096335. <https://doi.org/10.1029/2021GL096335>
- Kasper, J. C., Lazarus, A. J., & Gary, S. P. (2008). Hot solar-wind helium: Direct evidence for local heating by Alfvén-cyclotron dissipation. *Physical Review Letters*, *101*(26), 261103. <https://doi.org/10.1103/PhysRevLett.101.261103>
- Kitamura, N., Omura, Y., Nakamura, S., Amano, T., Boardsen, S. A., Ahmadi, N., et al. (2020). Observations of the source region of whistler mode waves in magnetosheath mirror structures. *Journal of Geophysical Research: Space Physics*, *125*(5). <https://doi.org/10.1029/2019JA027488>
- Klein, K. G., Martinović, M., Stansby, D., & Horbury, T. S. (2019). Linear stability in the inner heliosphere: Helios Re-evaluated. *ApJ*, *887*(2), 234. <https://doi.org/10.3847/1538-4357/ab5802>
- Klein, K. G., Verniero, J. L., Alterman, B., Bale, S., Case, A., Kasper, J. C., et al. (2021). Inferred linear stability of parker solar probe observations using one- and two-component proton distributions. *ApJ*, *909*(1), 7. <https://doi.org/10.3847/1538-4357/abd7a0>
- Kunz, M. W., Schekochihin, A. A., & Stone, J. M. (2014). Firehose and mirror instabilities in a collisionless shearing plasma. *Physical Review Letters*, *112*(20), 205003. <https://doi.org/10.1103/PhysRevLett.112.205003>
- Lewis, H. C., Stawarz, J. E., Matteini, L., Franci, L., Klein, K. G., Wicks, R. T., et al. (2024). Turbulent energy conversion associated with kinetic microinstabilities in earth's magnetosheath. *Geophysical Research Letters*, *51*(24). <https://doi.org/10.1029/2024gl112038>
- Ley, F., Zweibel, E. G., Riquelme, M., Sironi, L., Miller, D., & Tran, A. (2023). A heating mechanism via magnetic pumping in the intracluster medium. *ApJ*, *947*(2), 89. <https://doi.org/10.3847/1538-4357/acb3b1>
- Li, H., Jiang, W., Wang, C., Verscharen, D., Zeng, C., Russell, C. T., et al. (2020). Evolution of the earth's magnetosheath turbulence: A statistical study based on MMS observations. *ApJ*, *898*(2), L43. <https://doi.org/10.3847/2041-8213/aba531>
- Li, H., Jiang, W., Yang, Z., Liu, X., Verscharen, D., & Wang, C. (2024). Pickup ion modulation on plateau-like turbulence in the martian magnetosheath. *ApJ*, *967*(2), 76. <https://doi.org/10.3847/1538-4357/ad3d49>
- Lichko, E., & Egedal, J. (2020). Magnetic pumping model for energizing superthermal particles applied to observations of the Earth's bow shock. *Nature Communications*, *11*(1), 2942. <https://doi.org/10.1038/s41467-020-16660-4>
- Liu, T. Z., Hao, Y., Wilson, L. B., Turner, D. L., & Zhang, H. (2021). Magnetospheric Multiscale observations of earth's oblique bow shock reformation by foreshock ultralow-frequency waves. *Geophysical Research Letters*, *48*(2), e2020GL091184. <https://doi.org/10.1029/2020GL091184>
- Lucek, E. A., Dunlop, M. W., Horbury, T. S., Balogh, A., Brown, P., Cargill, P., et al. (2001). Cluster magnetic field observations in the magnetosheath: Four-point measurements of mirror structures. *Annales Geophysicae*, *19*(10/12), 1421–1428. <https://doi.org/10.5194/angeo-19-1421-2001>
- Lucek, E. A., Horbury, T. S., Dandouras, I., & Rème, H. (2008). Cluster observations of the earth's quasi-parallel bow shock: Cluster at the parallel bow shock. *Journal of Geophysical Research*, *113*(A7). <https://doi.org/10.1029/2007JA012756>
- Maruca, B. A., Chasapis, A., Gary, S. P., Bandyopadhyay, R., Chhiber, R., Parashar, T. N., et al. (2018). MMS observations of beta-dependent constraints on ion temperature anisotropy in earth's magnetosheath. *The Astrophysical Journal*, *866*(1), 25. <https://doi.org/10.3847/1538-4357/aaddfb>
- Maruca, B. A., Kasper, J. C., & Bale, S. D. (2011). What are the relative roles of heating and cooling in generating solar wind temperature anisotropies? *Physical Review Letters*, *107*(20), 201101. <https://doi.org/10.1103/PhysRevLett.107.201101>
- McManus, M. D., Klein, K. G., Bale, S. D., Bowen, T. A., Huang, J., Larson, D., et al. (2024). Proton- and alpha-driven instabilities in an ion cyclotron wave event. *ApJ*, *961*(1), 142. <https://doi.org/10.3847/1538-4357/ad05ba>
- Papitashvili, N., Bilitza, D., & King, J. (2014). Omni: A description of near-earth solar wind environment. In *40th cospar scientific assembly*. Vol. 40, p. C0.1-12-14.
- Perri, S., Perrone, D., Yordanova, E., Sorriso-Valvo, L., Paterson, W. R., Gershman, D. J., et al. (2020). On the deviation from Maxwellian of the ion velocity distribution functions in the turbulent magnetosheath. *Journal of Plasma Physics*, *86*(1), 905860108. <https://doi.org/10.1017/S0022377820000021>
- Pollock, C., Moore, T., Jacques, A., Burch, J., Gliese, U., Saito, Y., et al. (2016). Fast plasma investigation for magnetospheric Multiscale. *Space Science Reviews*, *199*(1–4), 331–406. <https://doi.org/10.1007/s11214-016-0245-4>
- Preisser, L., Blanco-Cano, X., Kajdič, P., Burgess, D., & Trotta, D. (2020). Magnetosheath jets and plasmoids: Characteristics and formation mechanisms from hybrid simulations. *The Astrophysical Journal*, *900*(1), L6. <https://doi.org/10.3847/2041-8213/abad2b>
- Quest, K. B., & Shapiro, V. D. (1996). Evolution of the fire-hose instability: Linear theory and wave-wave coupling. *Journal of Geophysical Research*, *101*(A11), 24457–24469. <https://doi.org/10.1029/96JA01534>
- Rakhmanova, L. S., Riazantseva, M. O., Zastenker, G. N., & Verigin, M. I. (2018). Effect of the magnetopause and bow shock on characteristics of plasma turbulence in the earth's magnetosheath. *Geomagnetism and Aeronomy*, *58*(6), 718–727. <https://doi.org/10.1134/S0016793218060129>
- Rezeau, L., Belmont, G., Cornilleau-Wehrlin, N., Reberac, F., & Briand, C. (1999). Spectral law and polarization properties of the low-frequency waves at the magnetopause. *Geophysical Research Letters*, *26*(6), 651–654. (WOS:000079207400007). <https://doi.org/10.1029/1999GL900060>
- Russell, C. T., Anderson, B. J., Baumjohann, W., Bromund, K. R., Dearborn, D., Fischer, D., et al. (2016). The magnetospheric Multiscale magnetometers. *Space Science Reviews*, *199*(1–4), 189–256. <https://doi.org/10.1007/s11214-014-0057-3>
- Sahraoui, F., Belmont, G., Rezeau, L., Cornilleau-Wehrlin, N., Pinçon, J. L., & Balogh, A. (2006). Anisotropic turbulent spectra in the terrestrial magnetosheath as seen by the cluster spacecraft. *Physical Review Letters*, *96*(7), 075002. <https://doi.org/10.1103/PhysRevLett.96.075002>

- Santolík, O., Parrot, M., & Lefeuvre, F. (2003). Singular value decomposition methods for wave propagation analysis: SVD methods for wave propagation analysis. *Radio Science*, 38(1). <https://doi.org/10.1029/2000RS002523>
- Schwartz, S. J., & Burgess, D. (1991). Quasi-parallel shocks: A patchwork of three-dimensional structures. *Geophysical Research Letters*, 18(3), 373–376. <https://doi.org/10.1029/91GL00138>
- Schwartz, S. J., Burgess, D., & Moses, J. J. (1996). Low-frequency waves in the Earth's magnetosheath: Present status. *Ann. Geophys.-Atmos. Hydrospheres Space Sci.*, 14(11), 1134–1150. (WOS:A1996VT49000005. <https://doi.org/10.1007/s005850050376>
- Sckopke, N., Paschmann, G., Bame, S. J., Gosling, J. T., & Russell, C. T. (1983). Evolution of ion distributions across the nearly perpendicular bow shock: Specularly and non-specularly reflected-gyrating ions. *Journal of Geophysical Research: Space Physics*, 88(A8), 6121–6136. <https://doi.org/10.1029/JA088iA08p06121>
- Shue, J.-H., Chao, J. K., Fu, H. C., Russell, C. T., Song, P., Khurana, K. K., & Singer, H. J. (1997). A new functional form to study the solar wind control of the magnetopause size and shape. *Journal of Geophysical Research: Space Physics*, 102(A5), 9497–9511. <https://doi.org/10.1029/97JA00196>
- Song, P., & Russell, C. (1997). What do we really know about the magnetosheath? *Advances in Space Research*, 20(4–5), 747–765. [https://doi.org/10.1016/S0273-1177\(97\)00466-3](https://doi.org/10.1016/S0273-1177(97)00466-3)
- Soucek, J., Escoubet, C. P., & Grison, B. (2015). Magnetosheath plasma stability and ULF wave occurrence as a function of location in the magnetosheath and upstream bow shock parameters. *Journal of Geophysical Research: Space Physics*, 120(4), 2838–2850. <https://doi.org/10.1002/2015JA021087>
- Soucek, J., Lucek, E., & Dandouras, I. (2008). Properties of magnetosheath mirror modes observed by cluster and their response to changes in plasma parameters: Mirror mode properties. *Journal of Geophysical Research*, 113(A4). <https://doi.org/10.1029/2007JA012649>
- Southwood, D. J., & Kivelson, M. G. (1993). Mirror instability: 1. Physical mechanism of linear instability. *Journal of Geophysical Research*, 98(A6), 9181–9187. <https://doi.org/10.1029/92JA02837>
- Turc, L., Roberts, O. W., Verscharen, D., Dimmock, A. P., Kajdič, P., Palmroth, M., et al. (2023). Transmission of foreshock waves through Earth's bow shock. *Nature Physics*, 19(1), 78–86. <https://doi.org/10.1038/s41567-022-01837-z>
- Verigin, M., Tátrallyay, M., Erdős, G., & Kotova, G. (2006). Magnetosheath – Interplanetary medium reference frame: Application for a statistical study of mirror type waves in the terrestrial plasma environment. *Advances in Space Research*, 37(3), 515–521. <https://doi.org/10.1016/j.asr.2005.03.042>
- Verscharen, D., Chandran, B. D. G., Klein, K. G., & Quataert, E. (2016). Collisionless isotropization of the solar-wind protons by compressive fluctuations and plasma instabilities. *The Astrophysical Journal*, 831(2), 128. <https://doi.org/10.3847/0004-637X/831/2/128>
- Verscharen, D., Klein, K. G., & Maruca, B. A. (2019). The multi-scale nature of the solar wind. *Living Reviews in Solar Physics*, 16(1), 5. <https://doi.org/10.1007/s41116-019-0021-0>
- Walters, J., Klein, K. G., Lichko, E., Stevens, M. L., Verscharen, D., & Chandran, B. D. G. (2023). The effects of nonequilibrium velocity distributions on Alfvén ion-cyclotron waves in the solar wind. *The Astrophysical Journal*, 955(2), 97. <https://doi.org/10.3847/1538-4357/acf1fa>
- Woodham, L. D., Wicks, R. T., Verscharen, D., Owen, C. J., Maruca, B. A., & Alterman, B. L. (2019). Parallel-propagating fluctuations at proton-kinetic scales in the solar wind are dominated by kinetic instabilities. *The Astrophysical Journal Letters*, 884(2), L53. <https://doi.org/10.3847/2041-8213/ab4adc>
- Yordanova, E., Vaivads, A., André, M., Buchert, S. C., & Vörös, Z. (2008). Magnetosheath plasma turbulence and its spatiotemporal evolution as observed by the cluster spacecraft. *Physical Review Letters*, 100(20), 205003. <https://doi.org/10.1103/PhysRevLett.100.205003>